Hindawi
Geofluids
Volume 2021, Article ID 5515665, 19 pages
https://doi.org/10.1155/2021/5515665

Research Article

Study of Characteristics of Fault Slip and Induced Seismicity during Hydraulic Fracturing in HDR Geothermal Exploitation in the Yishu Fault Zone in China

Zhiyong Niu[1], **Shiquan Wang**[1], **Hongrui Ma**[1], **Hengjie Luan**[2] and **Zhouyuyan Ding**[1]

[1]*School of Resources and Civil Engineering, Suzhou University, Suzhou 234000, China*
[2]*College of Energy and Mining Engineering, Shandong University of Science and Technology, Qingdao 266590, China*

Correspondence should be addressed to Zhiyong Niu; niuzhiyong88@ahszu.edu.cn

Received 16 February 2021; Revised 17 March 2021; Accepted 20 March 2021; Published 7 April 2021

Academic Editor: Chun Zhu

Hot dry rock (HDR) geothermal energy has become promising resources for relieving the energy crisis and global warming. The exploitation of HDR geothermal energy usually needs an enhanced geothermal system (EGS) with artificial fracture networks by hydraulic fracturing. Fault reactivation and seismicity induced by hydraulic fracturing raise a great challenge. In this paper, we investigated the characteristics of fault slip and seismicity by numerical simulation. The study was based on a hydraulic fracturing project in the geothermal field of Yishu fault zone in China. It revealed that fluid injection during hydraulic fracturing can cause the faults that exist beyond the fluid-pressurized region to slip and can even induce large seismic event. It was easier to cause felt earthquakes when hydraulic fracturing was carried out in different layers simultaneously. We also examined the effects of the location, permeability, and area of the fracturing region on fault slip and magnitude of the resulting events. The results of the study can provide some useful references for establishing HDR EGS in Yishu fault zone.

1. Introduction

With the global economic development, the increasing depletion of fossil resources such as petroleum, coal, and natural gas is very serious, accompanied by increasingly serious environmental problems such as environmental pollution and global warming. The energy crisis and global warming have become two major problems of the world today. Accelerating the exploitation of clean and renewable energy has become the goal of many countries around the world. Geothermal resources are renewable and low carbon, becoming promising energy resources for relieving the energy crisis and global warming. Among them, geothermal energy from hot dry rock (HDR), being regarded as an almost inexhaustible source of clean energy, has the biggest development potential. HDR resources refer to the rock mass with temperature above 150°C buried 3-10 km underground, having no or only a small amount of water [1]. The total heat energy within HDR worldwide is very huge. Just the HDR geothermal energy within the most easily accessible zone (less than 10 km deep) is up to 40-400 M quads (1 quad = 1.0551×10^{18} J), which is 100-1000 times than the available energy from all total fossil fuels worldwide [2]. HDR geothermal energy can be developed for heating generation which can be directly applied in domestic heating, aquaculture and agricultural heating, business and tourism heating (e.g., bathing and swimming), and other industrial uses. It can also be used for power generation. In addition to be clean and rich reserves, HDR geothermal is widely distributed and independent from variations in weather. Therefore, full exploitation of HDR heat resource plays an important role in energy supply and environmental protection for all countries in the world.

Cold fluid can be injected via injection wells into hot dry rocks and travels through them to capture the heat. The heated fluid then can be extracted to the surface via production to obtain heat energy. However, the natural HDR formations usually consist of hard and low-permeability granite.

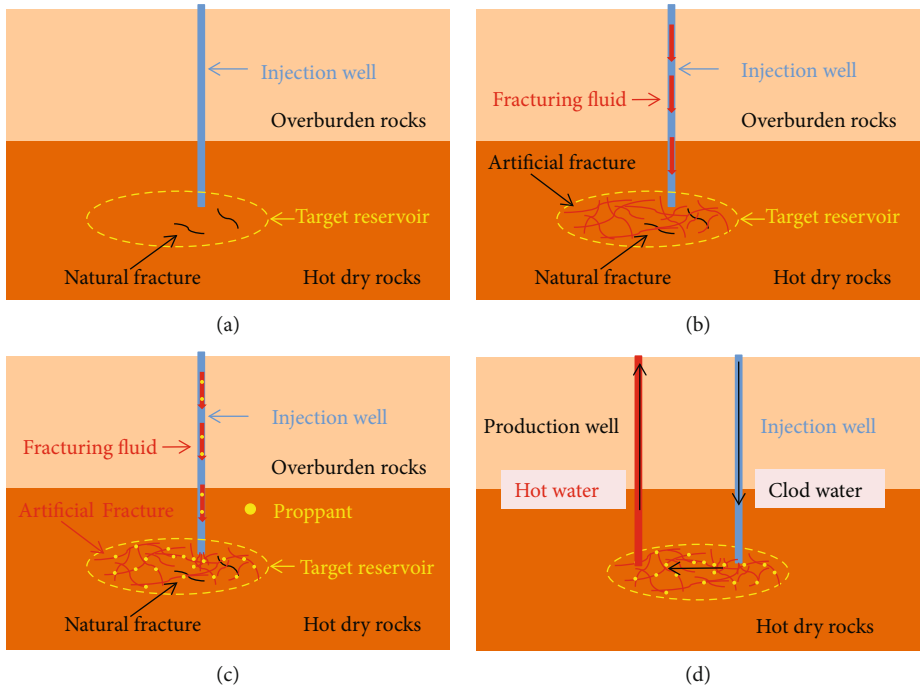

Figure 1: Schematic of EGS with artificial fracture networks by hydraulic fracturing.

Fluid cannot flow in them. Therefore, it is necessary to create artificial fracture networks in the HDR formations to improve their permeability to help the exploitation of the heat energy, which is called the enhanced geothermal system (EGS). The concept of EGS was first proposed in USA by Potter et al. (1974) as a patent in 1974 [3]. Hydraulic fracturing is one of the most significant technologies for establishing EGS in hot dry rocks [4]. Firstly, a well is drilled into the target region (Figure 1(a)). Secondly, high-pressure fracturing fluid (usually water) is pumped into rocks via the well to form cracks or open the natural joints/fractures in the rocks (Figure 1(b)). Thirdly, fracturing proppant (e.g., quartz sand) is injected into the fractures to avoid them reclosing and achieve sufficient and stable flow paths (Figure 1(c)) [5, 6]. Finally, cold fluid is injected via injection well and heated by circulation through the fractured region and then extracted via production well to the surface to deliver the captured heat for power generation or other uses (Figure 1(d)).

In the course of underground fluid injection, fault reactivation and induced seismicity often raise a great challenge for its development. It is usually considered as a result of the effective stress principle [7], where the increase in pore pressure reduces the effective stress on preexisting fault which may lead to shear failure and seismic events [8]. This means that the induced seismicity by fluid injection is regarded as a fluid structure interaction (FSI) problem. Only when the injected fluid flows into or through the fault zone (as fault I shown in Figure 2) can reduce its effective stress and induce seismicity [9, 10]. Influenced by the "principle of effective stress", the fluid-induced seismicity is usually interpreted as the overpore pressure reaching faults and triggering them slip [11]. Most previous studies have been based on this interpretation, no matter theory study [12–14], lab experimental

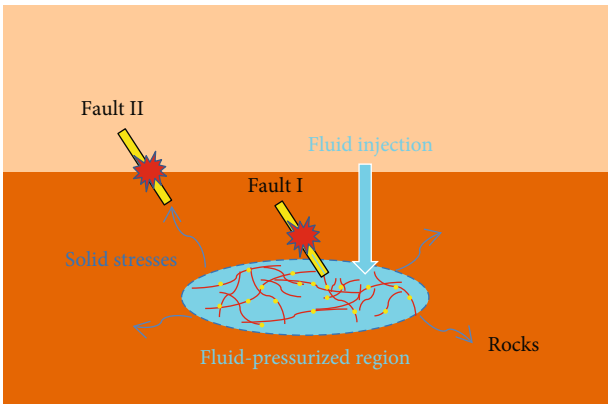

Figure 2: The diagram of the space relationship between the fault and fluid-pressurized region.

study [15], or numerical simulation study [16–18]. Earlier still, in 1959, Hubbert and Rubey concluded the over pore pressure would reduce the "effective strength of rock" and thus weaken the preexisting fault [19]. In 1978, M. Lee Bell and Amos Nur suggested the "rapid unloading may cause instantaneous crustal weakening owing to excess pore pressure" [20]. Over a long period in the past, the stability of faults that are not in the pore-fluid migration region (as fault II shown in Figure 2) has been neglected to a certain extent. However, more and more researches suggest that fluid injection can also induce fault slip [21] or even trigger seismicity [22, 23] outpaces pore-fluid migration. The overpressure decreased the effective stress of the injection region, leading it to an unloading state. The stress field of the region is changed, with the balance of initial stress in the surrounding rock mass being destroyed. Elasticity of rocks is an effective means

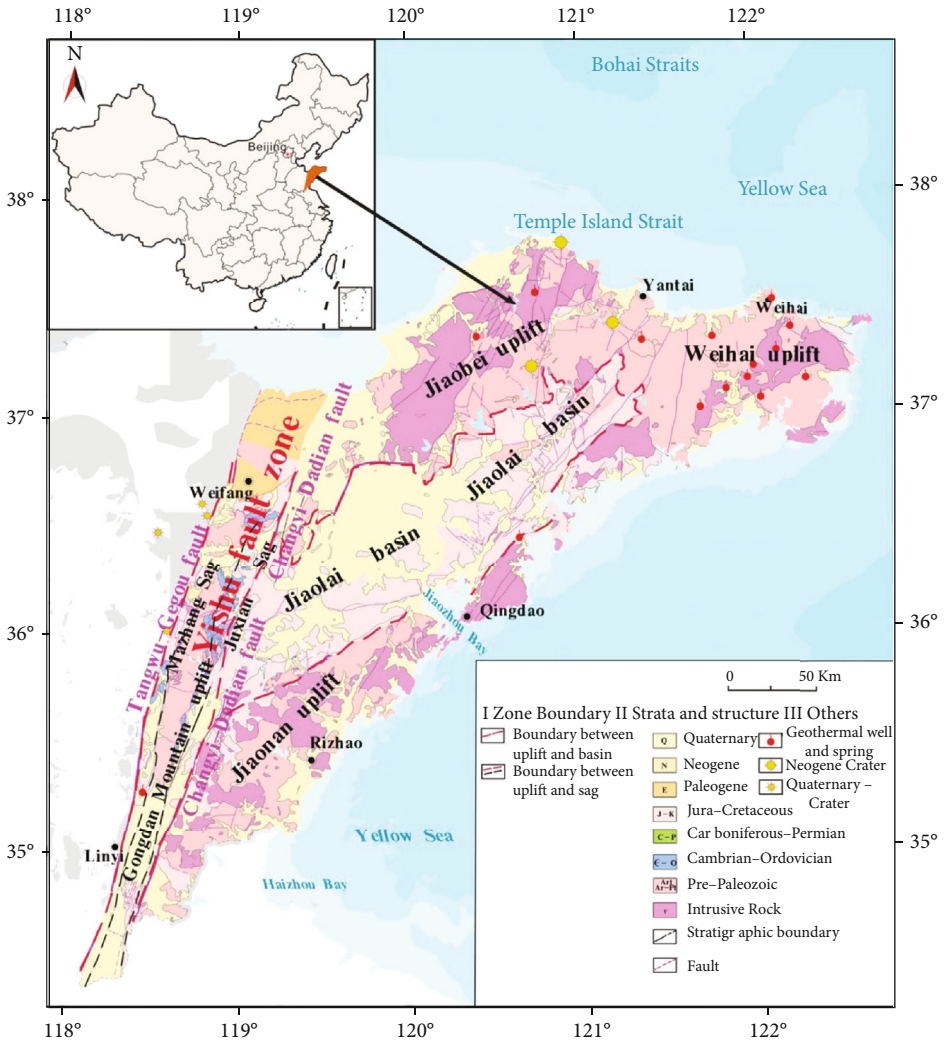

Figure 3: Location of the study area and distribution of geothermal geology [28].

of transmitting stresses to great distances [22]. The perturbation of stress field can spread to the faults and may cause them slip. Therefore, fluid injection induced fault slip, and seismicity outpaces pore-fluid migration which is a very important factor to be considered in a practical geothermal engineering.

Induced seismicity has also become a problem that must be considered in EGS which may cause fear and panic among local residents, especially after the November 2017 M_w 5.5 Pohang earthquake (South Korea) that has injured about 70 people and caused extensive damage in and around the city [24]. It will happen not only in the process of hydraulic circulation for heat recovery (as shown in Figure 1(d)) but also in the process of hydraulic fracturing (as shown in Figure 1(c)) [25].

China has a huge amount of HDR geothermal resources, about 23.69 M quads which is equivalent to 8.56 trillion tons of standard coal. It has become a strategic choice to ensure energy supply and social sustainable development [26]. In September 2017, dry hot rocks with temperature up to 236°C were drilled at 3705 m depth in Qinghai Gonghe Basin of China [25]. It is a major breakthrough in the exploration of dry hot rock, which directly confirmed that China has high quality dry hot rock resources. Favorable HDR resource development zones of China include Southern Tibet, Western Yunnan (Tengchong), Southeast Coast (Zhejiang, Fujian and Guangdong Provinces), North China (Bohai Bay Basin), on the southeast margin of Ordos Basin (Fenwei graben), and Northeast China (Songliao Basin), [27]. The east of the Yishu fault zone (Figure 3) is one of the best geothermal areas in Shandong Province [28]. In July 2019, a large number of dry hot rock rich areas (Ju County, Wulian County of Rizhao City and Wendeng District of Weihai City) have been found, having resources equivalent to 18.779 billion tons of standard coal. To establish the EGS in the Yishu fault zone and reduce the damage caused by induced seismicity, fault slip and induced seismicity characteristics during HDR geothermal exploitation in the Yishu fault zone were investigated in this paper by numerical simulation. Numerical simulation is an effective tool for solving problems of geotechnical engineering [29–31]. We used the finite-element software, ABAQUS, to estimate the induced fault slippage during hydraulic

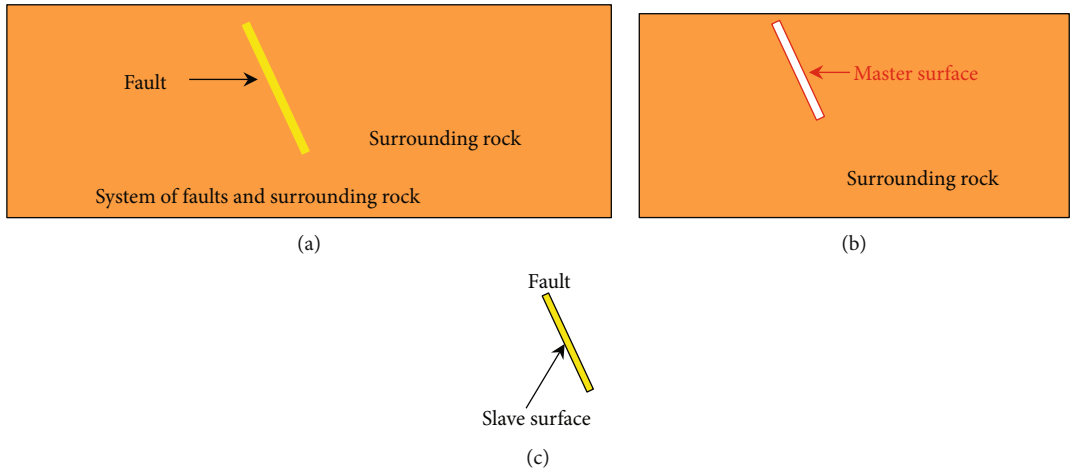

Figure 4: The master-slave surfaces of fault and its surrounding rock.

fracturing. ABAQUS has advantages in solving the inelastic, nonlinear, anisotropic, and heterogeneous problems.

Study on fault stability is vital for improving seismic hazard assessment and mitigation. In this paper, the study was focused on fault slip induced by fluid injection during the process of hydraulic fracturing (Figure 1(c)). In addition, we focused on the faults that exist beyond the hydraulic fracturing region. Considering a hydraulic fracturing case, we investigated the effects of fluid injection on stability of the selected faults through the following several aspects: (1) the influence of relative position between fracturing region and fault on induced fault ship and seismicity, (2) the influence of fracturing region's permeability on stability of the fault, (3) the influence of fluid injection pressure during hydraulic fracturing on stability of the fault, and (4) the influence of the area of the fracturing region on stability of the fault.

2. Numerical Method

2.1. Interaction between Fault and Its Surrounding Rock. The fault and its surrounding rock mass were treated as two parts (Figure 4(a)). Estimation of the induced fault slippage should well solve the interaction between the fault and surrounding rock. Contact analysis can be used to simulate the interaction between them. Contact is a special discontinuous constraint with nonlinear behavior of severe discontinuity. ABAQUS was selected to solve these problems due to its great advantages in dealing with nonlinear calculation [32].

2.1.1. Defining Contact Pair. Contact pair in ABAQUS was used to complete the contact analysis between the two deformable surfaces (fault and its surrounding rock). In the contact pair, force can be transferred through their interface. Normal force is transmitted along the vertical direction. When the contact pressure becomes zero or negative, the two surfaces will separate. Shear force can be transmitted along the tangential direction when there is friction between the two surfaces. The master-slave contact method was used to define the contact pair of the fault and surrounding rock. Before the definition of contact pair, it was needed to determine which one was the master surface and which one was the slave. According to the guidelines of "defining a surface-based contact simulation" in ABAQUS [32], the surface of THE surrounding rock was chosen as the master surface (Figure 4(b)), and the surface of fault was chosen as THE slave surface (Figure 4(c)). The reason was that the stiffness of the surrounding rock mass was larger than that of fault [30].

2.1.2. Defining Contact Properties. After the definition of contact pair, the properties of contact were needed to be defined. To avoid one surface penetrating to another, the "hard" contact was assigned in the normal direction of the interface of contact. The Coulomb friction model was used in the tangential direction. In this model, the two contacting surfaces can carry shear stresses up to a certain magnitude across their interface before they start sliding relative to one another. The Coulomb friction model defines this critical shear stress, τ_{cirt}, at which sliding of the surfaces starts as a fraction of the contact pressure, p, between the surfaces ($\tau_{\text{cirt}} = \mu p$, μ is the coefficient of friction) [32].

2.1.3. Contact Tracking Approach. It has two tracking approaches to account for the relative motion of two contacting surfaces in mechanical contact simulations: finite sliding and small sliding. In small-sliding formulation, only relatively small sliding relative to each other of the interacting surfaces is allowed. In the finite sliding formulation, however, any size of sliding is permitted. Small-sliding contact is computationally less expensive than finite-sliding contact. However, the degree of the induced fault slip along the surrounding rock often cannot predict in advance. Large slippage may also occur. Therefore, the finite sliding formulation was used for this study.

The contact is described by a node n_1 on the slave surface with a quadratic segment with nodes n_2, n_3, and n_4 (Figure 5). To derive the equations governing these elements, the coordinates in the plane of the slide line is considered. Firstly, the point x on the segment closest to the point x_1 on the slave surface is determined. Secondly, the normal n and tangent t to the segment at that point is determined.

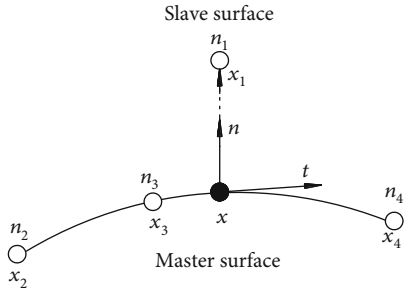

FIGURE 5: Quadratic slide line segment.

Then, point x and the normal n have the following relationship [32]:

$$nh = x - x_1, \tag{1}$$

where h is the overclosure.

The slip can be solved by the following equations:

$$d\delta h = -\delta x_i \bullet \left(n\frac{dN_i}{ds}N_j t + tN_i\frac{dN_j}{ds}n + tN_i\rho_n N_j t \right) dx_j, \tag{2}$$

$$d\delta s = \delta x_i \left(t\frac{dN_i}{ds}N_j t - nN_i\frac{dN_j}{ds}n - nN_i\rho_n N_j t \right) \bullet dx_j, \tag{3}$$

where s is the slip.

Detailed derivation of the equations can refer to ABAQUS theory manual [32].

2.2. Hydromechanical Coupling of the Hydraulic Fracturing Region. The process of fluid injection into the fracturing region was regarded as a problem of fluid-structure coupling. In this study, the simulation of the hydraulic fracturing region is based on porous elastic theory. The porous elastic medium is described by the flowing equations [33, 34]:

$$2G\varepsilon_{ij} = \sigma_{ij} - \frac{\nu}{(1+\nu)}\sigma_{kk}\delta_{ij} + \frac{3(\nu_u - \nu)}{B(1+\nu)(1+\nu_u)}p\delta_{ij}, \tag{4}$$

$$\Delta m = \frac{3\rho_0(\nu_u - \nu)}{2GB(1+\nu)(1+\nu_u)}(\sigma_{kk} + 3p/B), \tag{5}$$

$$B = \frac{1/K - 1/K_s}{1/K - 1/K_S + \left(1/K_f - 1/K_n\right)}, \tag{6}$$

where G is the shear modulus, ε_{ij} is the strain, σ_{ij} is the stress, σ_{kk} is the mean stress deviation, Pa, p is the pore pressure, Pa, ν_u and ν are undrained and drained Poisson's ratios, respectively, δ_{ij} is the Kronecker delta, Δm is the change in fluid mass per unit volume, kg/m^3, ρ_0 is the density of the pore fluid in the reference state, kg/m^3, B is Skempton's B coefficient, K and K_s are drained bulk modulus and solid grain's bulk modulus, and $1/K_n$ and K_f are the unjacketed pore compressibility and pore fluid bulk modulus, respectively.

The flow is described by Darcy's law and a mass conservation equation. Darcy's law describes the pore fluid flowing in a porous medium:

$$f = -\frac{\kappa}{\mu}\nabla p, \tag{7}$$

where f is the volumetric flux vector, m/s, κ is the intrinsic permeability of the medium, m^2, μ is the viscosity, Pa·s, and ∇p is the pressure gradient vector, Pa/m.

The mass conservation equation of pore fluid is [35]:

$$\frac{dK}{dt} + \nabla(\rho_0 \bullet f), \tag{8}$$

where K is the fluid mass.

2.3. The Induced Moment Magnitude of Fault. The slip of a preexisting fault will release a lot of energy. The amount of the energy depends on several factors, such as the size of the slipping fault, the mechanical properties of the fault, and its slip distance,. Seismic moment M_0 proposed by Aki (1967) can be used to quantify the released energy, as follows [36]:

$$M_0 = \mu A d, \tag{9}$$

where μ is the rigidity of fault, Pa, A is the fault rupture area and $A = lw$ (l and w are length and width of fault rupture, respectively), and d is the average slip of the rupture area.

On the base of seismic moment M_0, moment magnitude scale M_S proposed by Kanamori and Anderson (1975) can be calculated to measure the strength of the induced seismic event [37–39], as follows:

$$M_s = \frac{2}{3}(\log M_0 - 9.1). \tag{10}$$

3. Model Setup

3.1. Conceptual Model. A two-dimension model was designed to simulate the EGS-Fault system by ABAQUS [32]. A numerical model was simplified from a hydraulic fracturing field test in Yishu fault zone. We mainly investigated the characteristics of the fault slippage and seismicity induced by fluid injection during hydraulic fracturing of EGS engineering. According to geological exploration data, two major faults (named F1 and F2) that adjacent to but beyond the hydraulic fracturing region were selected. Contact analysis was used to describe the interaction behavior between the faults and the surrounding rock. Mohr–Coulomb failure criterion was used to control the slip of fault. A plane strain model with dimensions of 8,000 m × 400 m (Figure 6) was developed to simulate the geothermal system. The thicknesses of caprock and granite were 1000 m and 3000 m, respectively. Actually, the total caprock above granite was about 2000 m. In order to improve the simulation efficiency, the caprock in our model was only 1000 m. The other 1000 m caprock was replaced by the uniformly distributed

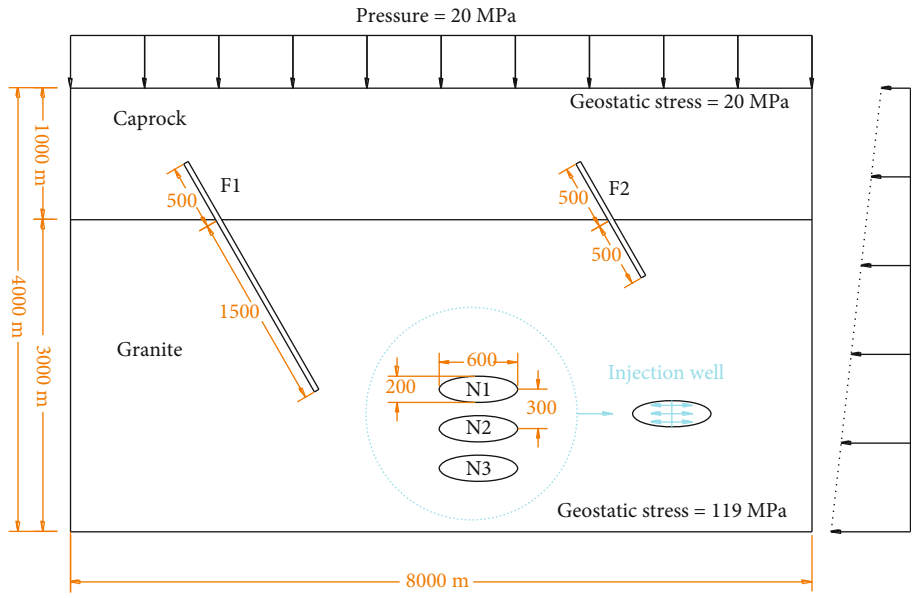

Figure 6: Model of hydraulic fracturing in HDR EGS engineering.

Table 1: Physical parameters of the rock mass.

Property	Density (kg/m^3)	Young's modulus (GPa)	Poisson's ratio (-)	Porosity (-)	Friction coefficient (-)	Permeability (m/s)
Caprock	2500	20	0.30	—	—	—
Granite	2800	50	0.15	—	—	—
Hydraulic fracturing region	2100	8	0.35	0.4	—	1×10^{-8}
Fault	2200	15	0.2	—	—	—

pressure that equals to its weight. The length of fault F1 was 2000 m, with the length in granite and caprock that was 1500 m and 500 m, respectively. The length of fault F2 is 1000 m, with the length in granite and caprock that is 500 m and 500 m, respectively. The thicknesses and inclinations of fault F1 and F2 were 10 m and 60°, respectively. In the field test, hydraulic fracturing was carried out in three different layers. As shown in Figure 6, three elliptic regions (regions N1, N2, and N3) were used to simulate the fracturing region in each layer. The long axis and short axis of the ellipse were 600 m and 200 m, respectively. The vertical distances from the center of regions N1, N2, and N3 to bottom of fault F1 were 0 m, 300 m and 600 m, respectively. The distance from the midpoint of the fracturing region N1 to the ground surface was 3600 m. The horizontal distance between the center of region N1 and the bottom of fault F1 was 1220 m. Injection well was a vertical well along the short axis of the ellipse region. The material properties of the model were mainly obtained from the logs and well data from the field as well as laboratory experiments, as shown in Table 1. The parameters that could not be measured were mainly determined from other public literature [40, 41].

The boundary conditions of model are (1) the bottom of the model was fixed, in which both vertical and horizontal displacement are not allowed, (2) the left and right sides of the model are constrained by rollers, only vertical displacement was allowed, and (3) the top of the model is allowed to deform freely.

The stress within the fault-stratum system should be equal to the lithostatic stress prior to hydraulic fracturing for geothermal exploitation. The initial stresses should be geostatic. Water pressure is hydrostatic within the hydraulic fracture region, with the initial value to be 0 MPa. Firstly, the gravity is considered as external force applied to the model. After the application of gravity, the stresses of each node are obtained. Secondly, the stresses are inputted to the model as initial internal force before gravity to reach a mechanical equilibrium between the initial stress fields and the gravity under the applied boundary conditions of the model. Then, fluid is injected into the ellipse region to simulate the process of hydraulic fracturing.

3.2. Numerical Experiments. Fault reactivation and slip are a complex mechanical behavior of fault and its surrounding rocks involving the interaction of total stresses, pore pressures, and temperature stresses [42]. In this study, we focused on the additional influence of pore pressure changes within the fracturing region on induced fault slippage and seismicity.

3.2.1. Location of Fracturing Region. Due to the low permeability of granite, the water exchange between the rock and

fracture is very weak. The injected fluid can only flow in the fracturing region. However, the fluid pressurization in the fracturing region can transmit solid stresses to the adjacent faults that may trigger seismic event. The location of the fracturing region will directly control the stress perturbation of fault zone and consequently affect its stability. Therefore, the location of the fracturing region is a very important engineering parameter that influences the stability of faults. Regions N1, N2, and N3 were the three actual fracturing regions in the field test of hydraulic fracturing. In order to fully study the influence of the location of the fracturing region on fault's stability, we designed three hypothetical fracturing regions (regions P1, P2, and P3) that were closer to fault F1 (Figure 7). Regions P1, P2, and P3 can be obtained by shifting N1, N2, and N3 to the left with 820 m, horizontally. The horizontal distance between the left endpoint of region P1 and the bottom of fault F1 was 100 m. The distance between region P1 and N1 was 220 m. In summary, a total of six hydraulic fracturing regions were designed. As shown in Table 2, a total of 8 numerical experiments (i.e., Nos. C1-C4 for current fracturing program and Nos. H1-H4 for hypothetical fracturing) were designed to study the effect of the location of fracturing region on stability of fault. The schematic of numerical experiments according to different fracturing regions was shown in Figure 7. In experiments of Nos. C1-C3 (Figures 8(a)–8(c)) and Nos. H1-H3 (Figures 8(e)–8(g)), hydraulic fracturing was carried out in only one layer. In No. C4 (Figure 8(d)) and No. H4 (Figure 8(h)), hydraulic fracturing was simultaneously carried out in the three different layers.

In these numerical experiments, all injection wells are vertical with the injection pressure of 80 MPa. After 120 hours of fluid injection, we obtained the slippage along the fault F1 and F2 (Figures 9–14). Based on them, the seismic moment magnitude M_w can be then calculated (Tables 3–5).

3.2.2. Permeability of the Fracturing Region. The engineering effect of an enhanced geothermal system is largely dependent on the permeability of the fracturing region. Too low or too high permeability will both reduce the thermal recovery effect. The permeability directly affects fluid flowing in the fracturing region. If the permeability is too low, the fluid flows very slowly which affects the heat recovery rate. If the permeability is too high, however, the fluid flows very fast which affects the heat absorption from HDR. The permeability will also significantly affect the pressure build-up in the fracturing region and then affect the stress perturbation of the adjacent faults. When the injection pressure and time are kept constant, the fracturing region permeability will become the key factor that affects the stability of fault. Therefore, the influence of fracturing region permeability on fault slip and induced seismicity needs to be investigated. Based on experiments No. C1 (Figure 8(a)), a total of 5 numerical experiments (Nos. C1K1-C1K5) of this section were designed by changing the fracturing region permeability from 10^{-10} m/s to 10^{-6} m/s (Table 6).

In these numerical experiments, all injection wells are vertical with the injection pressure of 80 MPa. After 120 hours of hydraulic fracturing by fluid injection, we obtained

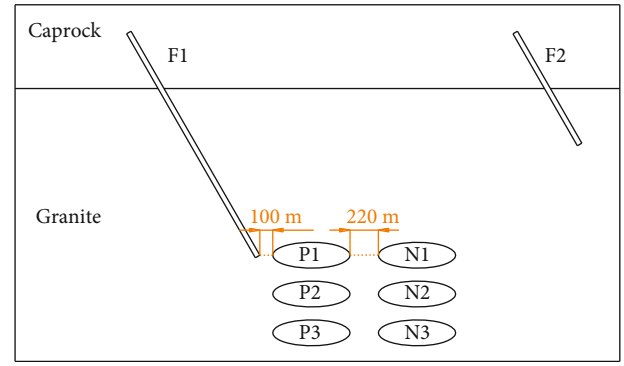

Figure 7: Schematic of different locations of the fracturing region.

Table 2: Numerical experiments according to different fracturing regions.

Experiment No.	Scenario	Fracturing region
C1	Current program	N1
C2		N2
C3		N3
C4		N1, N2, and N3
H1	Hypothetical program	P1
H2		P2
H3		P3
H4		P1, P2, and P3

the slippage along the faults F1 and F2 (Figures 15 and 16). Based on fault's slippage, the seismic moment magnitude can be then calculated (Table 7).

3.2.3. Injection Pressure. Injection pressure is another important factor that affects stress perturbation in the fracturing region and adjacent rocks. The internal pore pressure in the region increases rapidly when fluid is injected, reducing the effective stress of the region and leading it to an unloading state. The region will expand and cause the surrounding rock to lose stress balance. The stress perturbation may transfer to the nearby faults, which may induce them to loss stability. The influence of injection pressure on the induced fault slip and seismicity needs to be investigated. Based on the experiment No. C1, a total of 5 numerical experiments (Nos. C1P1-C1P5) of this section were designed by changing the injection pressure from 60 MPa to 70 MPa, 80 MPa, 90 MPa, and 100 MPa (Table 8).

In these numerical experiments, the permeability of the fracturing region is 10^{-10} m/s. All injection wells are vertical and after 120 hours of hydraulic fracturing by fluid injection, we obtained the slippage along the faults F1 and F2 (Figures 17 and 18). Based on fault's slippage, the seismic moment magnitude can be then calculated as shown in Table 9.

3.2.4. Area of the Fracturing Region. The size of the fracturing region can directly determine the area where the effective

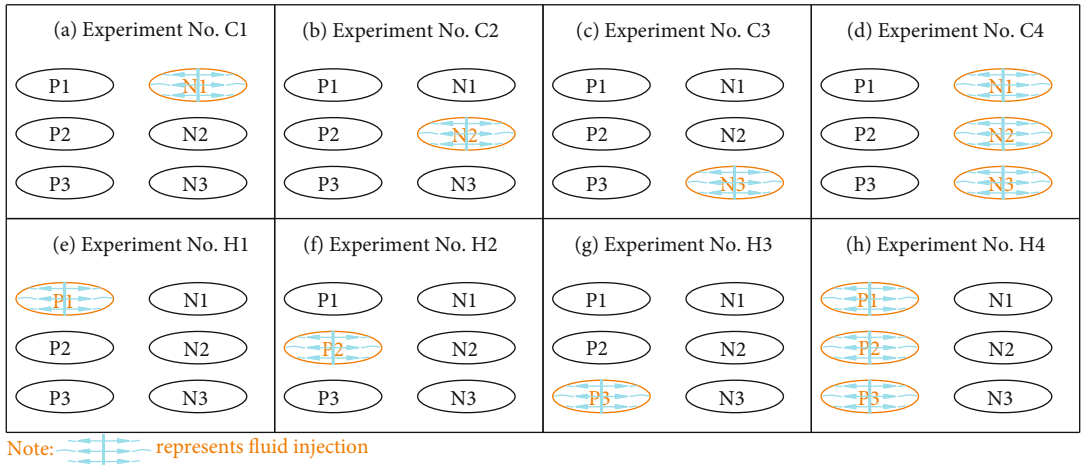

Figure 8: Schematic of numerical experiments according to different fracturing regions (experiments Nos. C1-C4 and Nos. H1-H4).

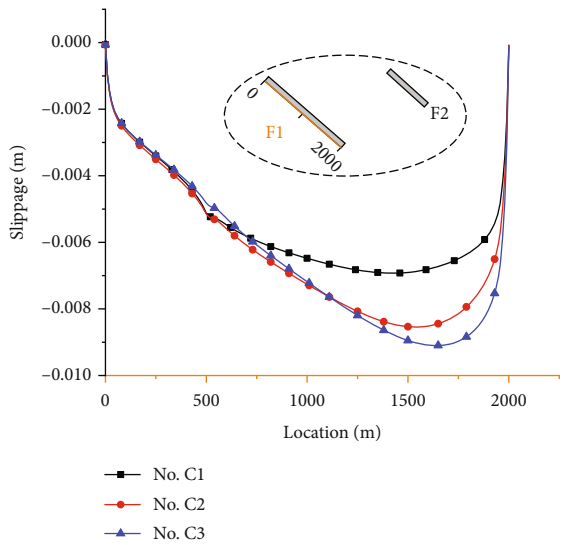

Figure 9: The fault slippage of F1 according to different fracturing regions (Nos. C1-C3).

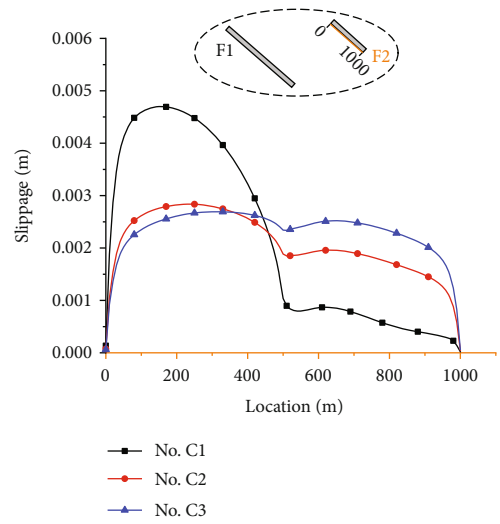

Figure 10: The fault slippage of F2 according to different fracturing regions (Nos. C1-C3).

stress changes, then affecting the stability of adjacent faults. Here, we investigated the influence of the area of the fracturing region on induced fault slip and seismicity. Region N3 (major axis of 600 m and minor axis of 200 m, with area of $A \approx 94,000\ m^2$) was selected as the basic model (experiments No. C3). Keeping the center of ellipse unchanged and decreasing (or increasing) both the long and short axes by 20%, we designed a total of 5 numerical experiments (Nos. C3A1-C3A5 as shown in Table 10). In these experiments, the fracturing region permeability and injection pressure were, respectively, remained constant at 10^{-8} m/s and 80 MPa. After 120 hours of fluid injection, we obtained the slippage along the faults F1 and F2 (Figures 19 and 20). The fault slippage and induced seismic moment magnitude M_w were as shown in Table 9.

4. Results and Discussion

4.1. Location of the Fracturing Region

4.1.1. Monolayer Fracturing

(1) Current Fracturing Program. Figures 9 and 10 illustrated the fault slippage along fault F1 (Figure 9) and F2 (Figure 10) of experiment Nos. C1-C3.

Firstly, we studied the induced slippage of fault F1. It can be seen that the induced slippage of fault F1 displayed similar tendency when hydraulic fracturing was implemented in regions N1, N2, and N3, respectively. (1) When the fracturing region was N1 (the black line with square symbol in Figure 9), fault F1 slipped downward along the fault plane. Maximum slip occurred at 1440 m, the lower portion of the fault plane. The maximal slippage was 6.93 mm, and the average slippage d was 5.34 mm. Then, the average slippage

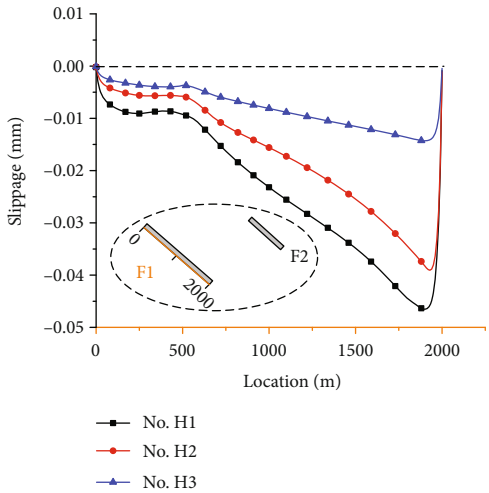

Figure 11: The fault slippage of F1 according to different fracturing regions (Nos. H1-H3).

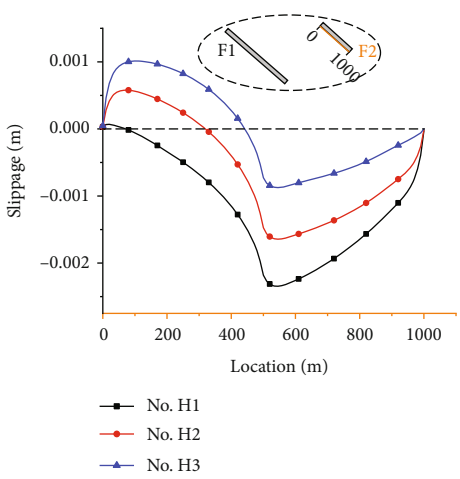

Figure 12: The fault slippage of F2 according to different fracturing regions (Nos. H1-H3).

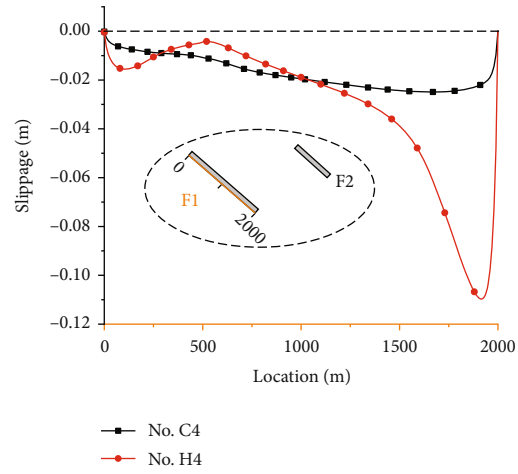

Figure 13: The fault slippage of F1 according to different fracturing regions (No. C4 and No. H4).

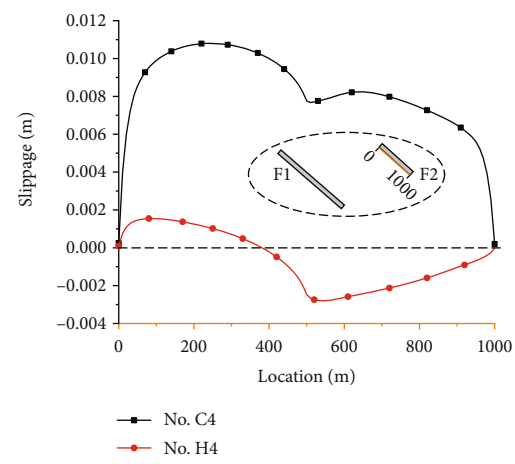

Figure 14: The fault slippage of F2 according to different fracturing regions (Nos. C4 and H4).

can be used to calculate the moment magnitude M_w of the induced seismicity of the induced earthquake. In our model, the shear modulus G of fault F1 can be calculated by its Young modulus (E) and Poisson's ratio (μ) by the equation of $G = E/2(1+\mu)$. The Young modulus of fault was 1.5×10^{10} Pa; Poisson's ratio was 0.2. Then, G was calculated to be 6.25×10^9 Pa. What we used in this study was a two-dimension model, and the length of fault plane F1 was 2000 m, but the width was unknown. According to the relevant observations and geological data, the width of the fault plane was assumed to be 200 m. Therefore, the rupture area A of F1 was 400,000 m^2. According to the above data and equation (10), the moment magnitude M_w of the induced seismicity of fault F1 was calculated to be 2.6837. (2) When the fracturing region was N2 (experiment No. C2), fault F1 also slipped downward along the fault plane (the blue line with triangle symbol in Figure 9). Maximum slip occurred at 1500 m, the lower portion of the fault plane. The maximal slippage was 8.54 mm, and the average slippage (d) was 6.00 mm. The moment magnitude M_w of the induced seismicity of fault F1 was 2.7174. (3) When the fracturing region was N3 (experiment No. C3), fault F1 also slipped downward along the fault plane (the red line with circle symbol in Figure 9). Maximum slip occurred at 1580 m, the lower portion of the fault plane. The maximal slippage was 9.10 mm, and the average slippage (d) was 6.06 mm. The moment magnitude M_w of the induced seismicity of fault F1 was 2.7203. When the fracturing region changed downward, the point of maximum slip of F1 moved downward, correspondingly. The induced slippage and moment magnitude M_w were obtained as shown in Table 3. The results were clearly inconsistent with our intuitive judgment. It was generally though that the influence of the hydraulic fracturing region on fault was larger, when it was closer to the fault. However, the results showed that the injection-induced fault slip became larger when the fracturing region changed downward. From the table, we can see that with the fracturing region changing

Table 3: The induced slippage and moment magnitude under different fracturing patterns of fault F1 and F2 (Experiment Nos. C1-C3).

Experiment No.	Fault F1			Fault F2		
	Maximal slippage (mm)	Average slippage (mm)	Moment magnitude (M_w)	Maximal slippage (mm)	Average slippage (mm)	Moment magnitude (M_w)
C1	6.93	5.34	2.6837	4.70	2.29	2.2378
C2	8.54	6.00	2.7174	2.84	2.14	2.2182
C3	9.10	6.06	2.7203	2.69	2.10	2.2128

Table 4: The induced slippage and moment magnitude under different fracturing patterns of faults F1 and F2 (Experiment Nos. H1-H3).

Experiment No.	Fault F1			Fault F2		
	Maximal slippage (mm)	Average slippage (mm)	Moment magnitude (M_w)	Maximal slippage (mm)	Average slippage (mm)	Moment magnitude (M_w)
P1	46.53	21.13	3.0819	2.35	1.00	1.9900
P2	39.06	15.11	2.9848	1.64	0.78	1.9260
P3	14.29	7.31	2.7746	1.01	0.62	1.8595

Table 5: The induced slippage and moment magnitude of faults F1 and F2 under different fracturing patterns.

Experiment No.	Fault F1			Fault F2		
	Maximal slippage (mm)	Average slippage (mm)	Moment magnitude (M_w)	Maximal slippage (mm)	Average slippage (mm)	Moment magnitude (M_w)
C4	24.90	16.20	3.0050	10.80	8.50	2.6176
H4	109.63	26.28	3.1450	2.80	1.40	2.0954

Table 6: Numerical experiments according to different permeability of the fracturing region.

Experiment No.	Fracturing region	Permeability of fracturing region
C1K1	N1	10^{-10}m/s
C1K2		10^{-9}m/s
C1K3		10^{-8}m/s
C1K4		10^{-7}/s
C1K5		10^{-6}m/s

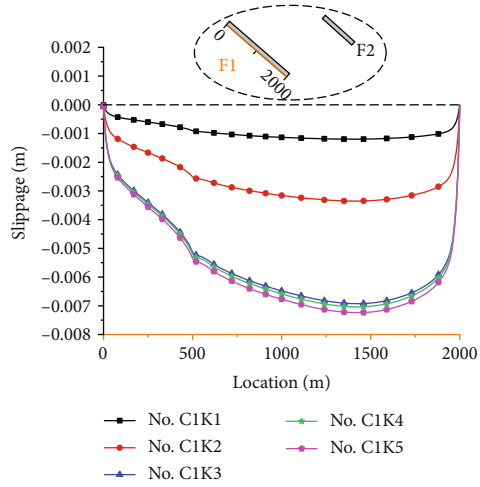

Figure 15: The fault slippage of F1 according to different permeability (Nos. C1K1-C1K5).

from N1 to N2 and then to N3, the induced slippage and moment magnitude of fault F1 both became larger. In fact, the influence of fluid injection on the adjacent faults' stability is not simply depended on the position of injection region, but on the stress disturbance region induced by it. It is the disturbance of stress and displacement field result from fluid injecting in the fracturing region that leads the fault slip. Figure 21 illustrated the distribution of vertical displacement of experiments Nos. C1 (Figure 21(a)), C2 (Figure 21(b)), and C3 (Figure 21(c)). When fluid was injected into the fracturing region, the region expanded, causing the upper surrounding rock to uplift and the lower surrounding rock to subside. The disturbance degree of the displacement field close to fault can directly affect its slid. When injection pressure and injection time remained constant, the displacement disturbance field close to the fracturing region kept the same. With the fracturing region changing from N1 to N2 and then to N3, the displacement disturbance field moved down, correspondingly. It may lead the displacement disturbance of fault F1 and its near area become much larger. Taking the displacement contour of U2 ≈ 0.1 m for example, it was approximate ellipse in the three experiments (as indicated by black dotted lines in Figure 21). When fluid was injected into regions N1, N2, and N3, the minimum distance between the contour and fault F1 was 780 m, 700 m, and 640 m, respectively. It meant that the displacement disturbance field

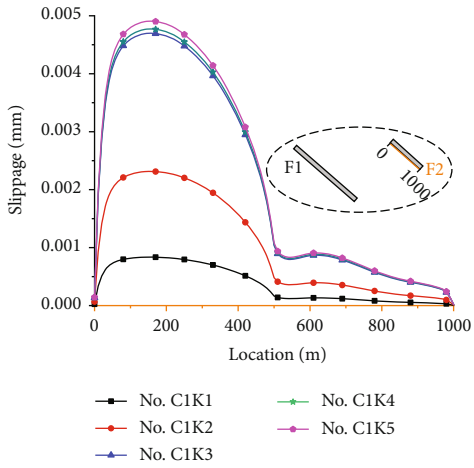

FIGURE 16: The fault slippage of F2 according to different permeability (Nos. C1K1-C1K5).

close to fault F1 became larger. This can explain why the moment magnitude M_w became larger when the fracturing region became far away the fault F1. Since the displacement contour of U2 ≈ 0.1 m was roughly elliptical, we could foresee that the distance between the contour and fault F1 would become smaller if the region continues to move down. Then, the moment magnitude M_w would not become larger. In contrast, it would become smaller. In order to verify this, we designed another numerical experiment by only moving region N3 down by 600 m to be N4 (the vertical distance from the center of N4 to the bottom of fault was then 1200 m). After 120 hours of fluid injection, we obtained the vertical displacement field and fault slippage as shown in Figures 22 and 23. When the fracturing region was N4, the maximal and average slippage of fault F1 was 8.21 mm (occurred at 1500 m of the fault plane) and 5.15 mm, respectively. The moment magnitude M_w was 2.6732, and it was smaller than that when fluid was injected into regions N1, N2, or N3.

Secondly, we studied the induced slippage along fault F2 (Figure 10). When fluid was injected into region N1, fault F2 slipped upward along the fault plane as shown in the black line with square symbol. The slippage along the upper half of the fault was obviously larger than that along the lower half. From 0 to 500 m, the maximal and average slippage was 4.70 mm and 3.80 mm, respectively. From 500 m to 1000 m, however, the maximal and average slippage was 4.70 mm and only 0.90 mm, respectively. As shown in the displacement cloud of No. C1 in Figure 21(a), the fluid-injection-induced displacement near the upper portion of the fault was larger than that near the lower portion. Along the whole fault plane of F2, the maximal slippage fault was 4.70 mm (occurred at 160 m) with the average slippage of 2.29 mm. The moment magnitude M_w of the induced seismicity of fault F2 was 2.2378. When fluid was injected into region N2, the displacement disturbance field moved down along with the fracturing region (as shown in Figure 21(b)). This caused the slippage along the upper portion of the fault to become smaller and that along lower portion of the fault to become larger. As shown in the red line with circle symbol in Figure 10, the difference of the slippage along the upper and lower part of the fault became smaller. From 0 to 500 m, the maximal and average slippage was 2.84 mm and 2.52 mm, respectively. From 500 m to 1000 m, the maximal and average slippage was 1.96 mm and only 1.67 mm, respectively. Along the whole fault plane of F2, the maximal and average slippage of fault F2 was 2.84 mm (occurred at 250 m of the fault plane) and 2.14 mm, respectively. The moment magnitude M_w of the induced seismicity of fault F2 was 2.2182. When fluid was injected into region N3, the induced slippage of fault F2 displayed similar tendency. The maximal and average slippage of fault F2 was 2.69 mm (occurred at 250 m of the fault plane) and 2.10 mm, respectively. The moment magnitude M_w of the induced seismicity of fault F2 was 2.2128. From Table 3, we can see that when the fracturing region changing from N1, N2, to N3, the induced slippage and moment magnitude M_w of fault F2 both became smaller. It was contrary to that of fault F1. That was because when the fracturing region changing from N1, N2, to N3, the displacement disturbance close to fault F2 became smaller.

The above results revealed that the influence of the hydraulic fracturing region on stability of fault was not simply depended on their relative spatial location. It was the displacement and stress disturbance induced by fluid injection in the fracturing region that ultimately caused the fault sliding instability.

(2) Hypothetical Fracturing Program. Figure 11 shows the fault slippage of fault F1 of experiment Nos. H1-H3. The induced slippage of fault F1 in the three experiments displayed similar tendency. The slippage along the upper portion of the fault was obviously smaller than that along the lower portion. Because the hypothetical fracturing region was near the bottom of fault F1, the disturbance degree of stress and displacement in the lower portion of fault F1 and its adjacent area was larger. Taking experiment No. H1 for example, as shown in Figure 24, the vertical displacement of the lower portion fault F1 and its adjacent area was obvious larger than that in upper portion. When fluid was injected into region P1 (the black line with square symbol in the Figure), the average slippage was 12.10 mm along 0-1000 m but it was 34.30 mm along 1000-2000 m. Along the whole fault plane, the maximal slippage of fault F1 was up to 46.53 mm, occurring at 1900 m of the fault plane. The average slippage was 21.13 mm, with the induced moment magnitude being up to 3.0819. When fluid was injected into region P2 (experiment No. H2, red line with circle symbol in the figure), the maximal and average slippage of fault F1 was 36.06 mm (occurred at 1930 m of the fault plane) and 15.11 mm, respectively. The moment magnitude M_w was 2.9848. When fluid was injected into region P3 (experiment No. H3, blue line with triangle symbol in the figure), the maximal and average slippage of fault F1 was 14.29 mm (occurred at 1930 m of the fault plane) and 7.31 mm, respectively. The moment magnitude M_w was 2.7746. The induced slippage and moment magnitude M_w were obtained as shown in Table 4. The results indicated that (1) when the

Table 7: The induced slippage and moment magnitude of faults F1 and F2 under different permeability of the fracturing region.

Experiment No.	Fault F1			Fault F2		
	Maximal slippage (mm)	Average slippage (mm)	Moment magnitude (M_w)	Maximal slippage (mm)	Average slippage (mm)	Moment magnitude (M_w)
C1K1	1.20	0.93	2.1779	0.84	0.40	1.7302
C1K2	3.35	2.60	2.4752	2.32	1.11	2.0286
C1K3	6.93	5.34	2.6837	4.70	2.29	2.2380
C1K4	7.04	5.43	2.6884	4.77	2.33	2.2427
C1K5	7.24	5.58	2.6964	4.91	2.39	2.2506

Table 8: Numerical experiments according to different injection pressures.

Experiment no.	Fracturing region	Injection pressure
C1P1		60 MPa
C1P2		70 MPa
C1P3	N1	80 MPa
C1P4		90 MPa
C1P5		100 MPa

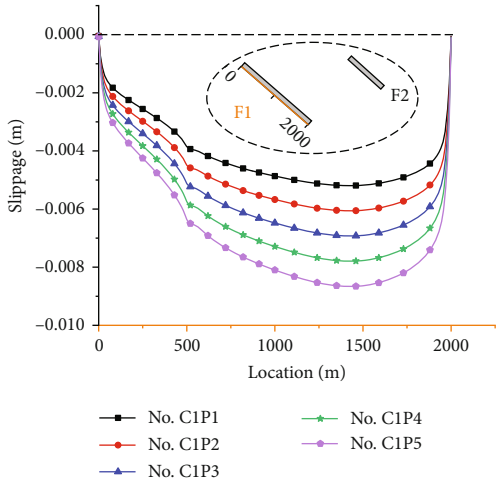

Figure 17: The fault slippage of F1 of different injection pressures (Nos. C1P1-C1P5).

fracturing region changed from P1 to P2 and then to P3, the induced slippage and moment magnitude M_w of fault F1 became smaller. It was different to that when fluid was injected into regions N1, N2, and N3, respectively. This can be also explained by the vertical displacement cloud as shown in Figure 24. With the fracturing region changing from N1 to N2 and N3, the range and degree of displacement disturbance in the lower portion of fault F1 and its adjacent area became smaller. (2) If the fracturing region was too close to the fault, as the region P1, injecting fluid into this region may induce felt seismic event ($M_w \geq 3$). Therefore, determination of rational position of fracturing region in HDR EGS engineering is a key step for site stability.

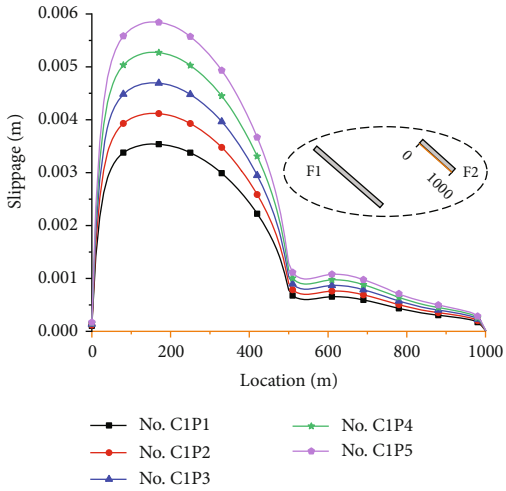

Figure 18: The fault slippage of F2 of different injection pressures (Nos. C1P1-C1P5).

Figure 12 illustrates the fault slippage of fault F2 of experiment Nos. H1-H3. The induced slippage of fault F2 also displayed similar tendency. The slippage curves all presented two sections, slipping upward along the upper portion and slipping downward along the lower portion. When fluid was injected into region P1, the fault plane slipped upward from 0 m to 70 m and downward from 70 m to 1000 m. This scenario resulted stretching at the position of 70 m, which was prone to damage. When fluid was injected into region P2, fault F2 slipped upward along 0-310 m and slipped downward along 310-1000 m. When fluid was injected into region P3, fault F2 slipped upward along 0-440 m and slipped downward along 440-1000 m. It revealed that with the fracturing region changing downward, the region of fault F2 that slipped upward became larger. From Table 4, it can be seen that the maximal slippages of fault F2 in Experiment Nos. H1-H3 were 2.35 mm, 1.64 mm, and 1.01 mm, respectively. The average slippage was 1.00 mm, 0.78 mm, and 0.62 mm, respectively. Accordingly, the moment magnitude M_w of the induced seismicity of induced seismicity was 1.99, 1.9260, and 1.8595, respectively. Because the fracturing regions P1-P3 were far from fault F2, the induced fault slippage and moment magnitude M_w were very small.

4.1.2. Multilayer Fracturing. Figure 13 illustrates the slippage of fault F1 when fluid was simultaneously injected into three

Table 9: The induced slippage and moment magnitude of faults F1 and F2 under different fracturing patterns.

Experiment No.	Fault F1			Fault F2		
	Maximal slippage (mm)	Average slippage (mm)	Moment magnitude (M_w)	Maximal slippage (mm)	Average slippage (mm)	Moment magnitude (M_w)
C1P1	5.20	4.01	2.6007	3.54	1.73	2.1566
C1P2	6.06	4.68	2.6455	4.12	2.01	2.2001
C1P3	6.93	5.34	2.6837	4.70	2.29	2.2378
C1P4	7.79	6.01	2.7179	5.28	2.57	2.2712
C1P5	8.66	6.67	2.7480	5.85	2.85	

Table 10: Numerical experiments according to different fracturing region areas.

Experiment No.	Size of elliptical fracturing region		Fracturing region area
	Major axis	Minor axis	
C3A1	360 m	120 m	0.36 A
C3A2	480 m	160 m	0.64 A
C3A3	600 m	200 m	A
C3A4	720 m	240 m	1.44 A
C3A5	840 m	280 m	1.96 A

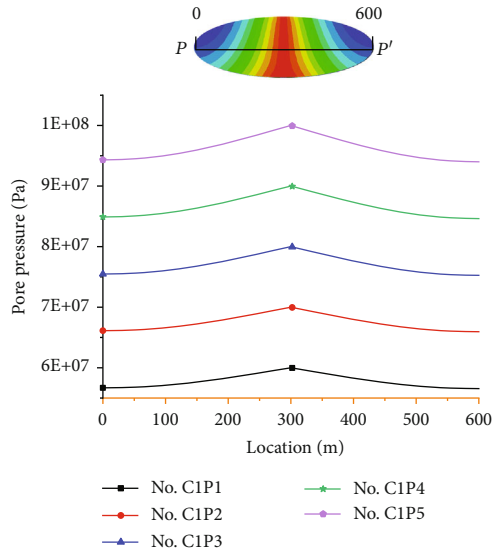

Figure 19: Pore pressure profiles along the long axis of region N1 (PP′) of different injection pressures (Nos. C1P1-C1P5).

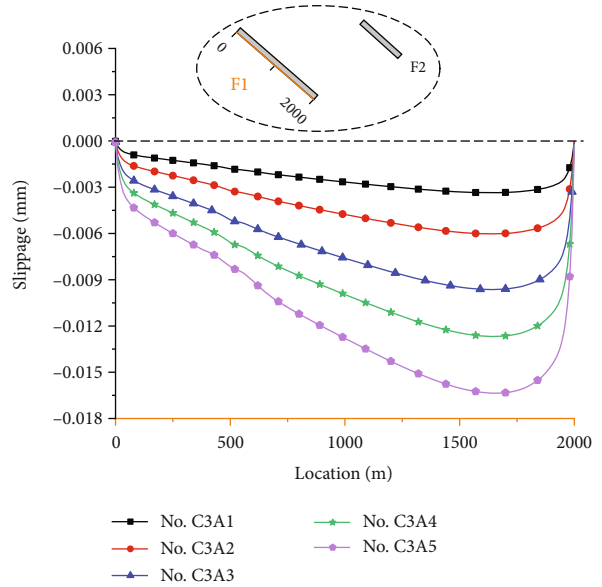

Figure 20: The induced fault slippage of F1 of different fracturing region areas (Nos. C1A1-C1A5).

different layers (experiments No. C4 and No. H4). Fault F1 slipped downward along the whole fault plane. When hydraulic fracturing was simultaneously carried out in regions N1, N2, and N3 (No. C4, black line with square symbol), the slippage along the whole fault plane was obvious larger than monolayer fracturing (N1, N2, or N3). The maximal slippage was up to 24.90 mm (occurred at 1460 m), and the average slippage was 16.20 mm. The moment magnitude M_w was 3.0050. When hydraulic fracturing was simultaneously carried out in regions P1-P3 (No. H4, red line with circle symbol), the slippage along the lower portion of the fault plane was obviously larger than that along the upper portion. In this case, the average slippage was 10.80 mm along 0-1000 m but was 48.41 mm along 1000-2000 m. The maximal slippage along the whole fault plane was up to 109.63 mm (occurred at 1920 m, near the bottom), with the average slippage up to 16.20 mm. In this case, the moment magnitude M_w was 3.1450.

Figure 14 illustrates the induced fault slippage of F2 of experiments No. C4 and No. H4. Fault F2 slipped downward along the whole fault plane in experiment No. C4. However, in experiment No. H4, it presented two sections with slipping upward along the upper portion and slipping downward along the lower portion. When fluid was injected into regions N1, N2, and N3 at the same time, the maximal slippage was 10.08 mm (occurred at 230 m), and the average slippage was 8.50 mm. In this case, the moment magnitude M_w was 2.6176. When fluid was injected into regions P1, P2, and P3 at the same time, the maximal slippage along the whole fault plane was only 2.80 mm, and the average slippage was 1.40 mm. The moment magnitude M_w was only 2.0954.

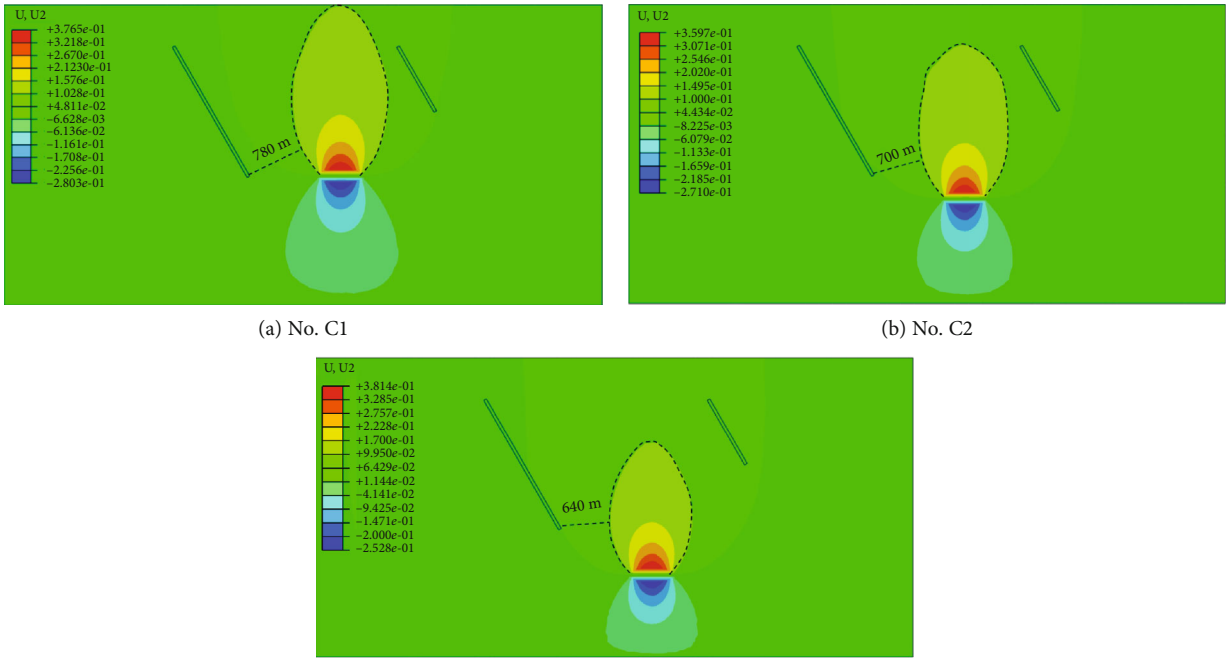

(a) No. C1

(b) No. C2

(c) No. C3

Figure 21: Distribution vertical displacement when fracturing region is N1 (a), N2 (b), and N3 (c).

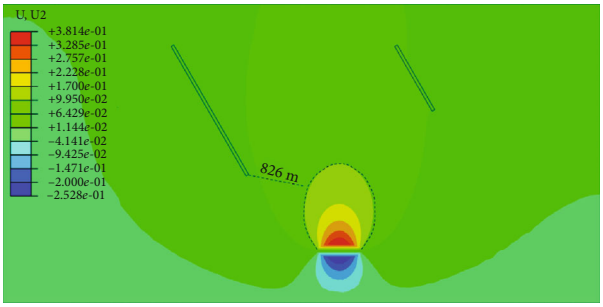

Figure 22: Distribution vertical displacement of when hydraulic fracturing region is N4 (No. C4).

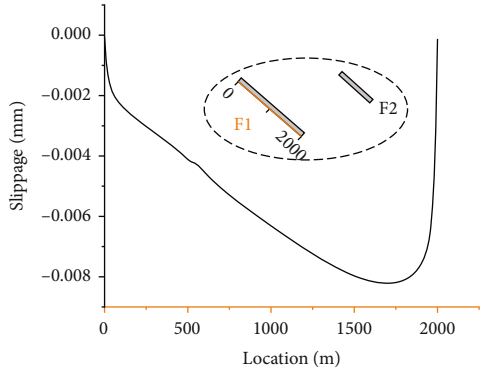

Figure 23: The fault slippage of F1 when the hydraulic fracturing region is N4.

Based on the results, the induced slippage and moment magnitude M_w were obtained as shown in Table 5. Comparing it with Tables 3 and 4, it can be seen that the induced fault slippage and moment magnitude M_w of experiment No. C4 were much larger than that of experiment Nos. C1-C3. It revealed that it was easier to cause felt earthquakes when hydraulic fracturing was carried out in different layers simultaneously. In the current hydraulic fracturing program, three different fracturing layers between fault F1 and F2 were set. It must be treated with caution when decided whether to carry out hydraulic fracturing in different layers at the same time.

4.2. Permeability of the Fracturing Region. Figures 15 and 16 and Table 7 show the results of the induced fault slippage and moment magnitude M_w of experiment Nos. C1K1-C1K5. When permeability of the fracturing region changed from 10^{-10} m/s to 10^{-6} m/s, the fault slippage and moment magnitude of fault F1 and F2 both showed an increasing tendency.

Firstly, we studied the induced fault slippage of F1 as shown in Figure 9 and Table 7. When the permeability was 10^{-10} m/s (the black curve with the symbol of square), the maximal and average-induced slippages were 1.20 mm and 0.93 mm, respectively. The moment magnitude M_w was 2.1779. When the permeability was 10^{-9} m/s (the red curve with the symbol of circle), the maximal and average-induced slippages were 3.35 mm and 2.60 mm, respectively. The moment magnitude M_w was 2.1779. When the permeability was 10^{-8} m/s (the blue curve with the symbol of triangle), the maximal and average-induced slippages were 6.93 mm and 5.34 mm, respectively. The moment magnitude M_w was 2.6837. When the permeability was 10^{-7} m/s (the green curve with the symbol of pentagram), the maximal and average-induced slippages were 7.04 mm and 5.43 mm, respectively. The moment magnitude M_w was 2.6884. When

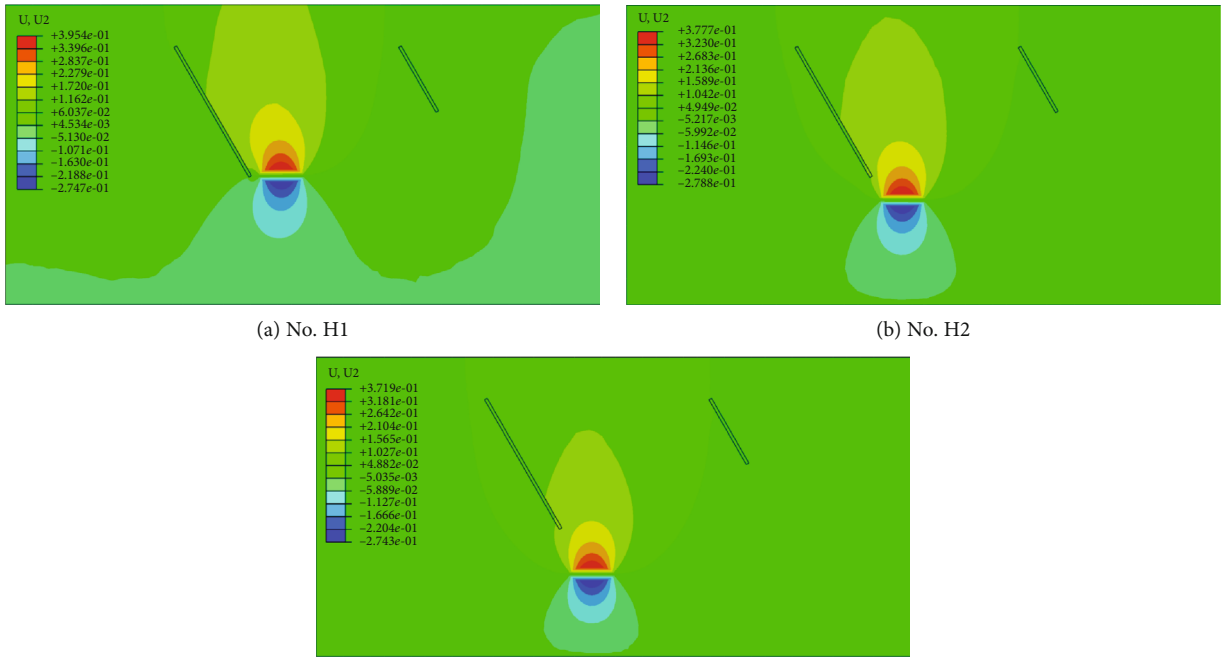

(a) No. H1

(b) No. H2

(c) No. H3

FIGURE 24: Distribution vertical displacement when the fracturing region is P1 (a), P2 (b), and P3 (c).

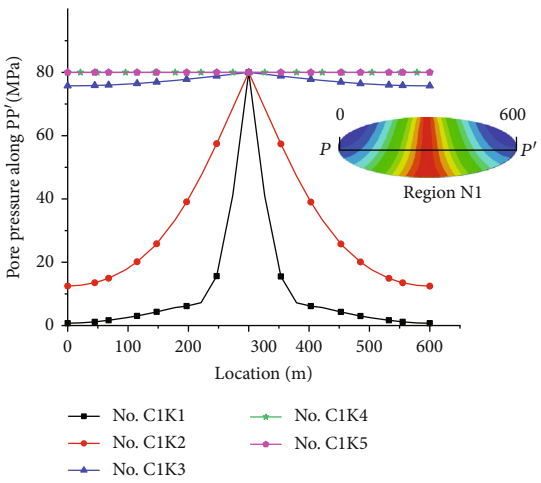

FIGURE 25: Pore pressure profiles along the long axis of region N1 (PP′) according to different permeability (Nos. C1K1-C1K5).

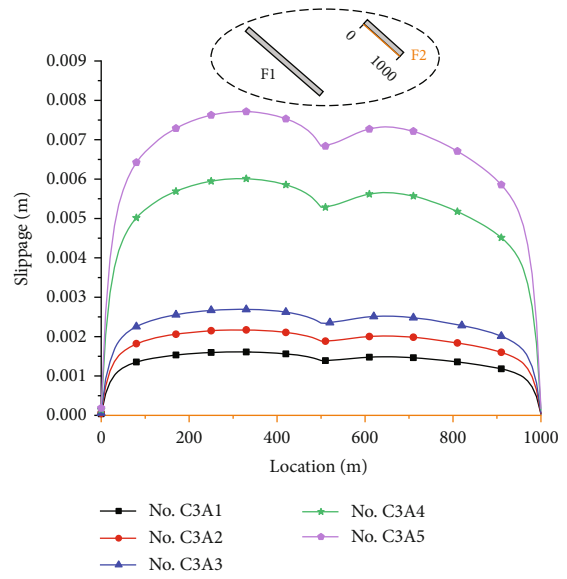

FIGURE 26: The induced fault slippage of F1 of different fracturing region areas (Nos. C1A1-C1A5).

the permeability was 10^{-6} m/s (the magenta curve with the symbol of regular pentagon), the maximal and average-induced slippages were 7.24 mm and 5.58 mm, respectively. The moment magnitude M_w was 2.6964.

Secondly, we studied the induced fault slippage of F2 as shown in Figure 16 and Table 7. When the permeability was 10^{-10} m/s, the maximal and average-induced slippages were 0.84 mm and 0.40 mm, respectively, with the moment magnitude M_w of the induced seismicity of 1.7302. When the permeability was 10^{-9} m/s, the maximal and average-induced slippages were 2.32 mm and 1.11 mm, respectively, with the moment magnitude M_w of the induced seismicity of 2.0286. When the permeability was 10^{-8} m/s, the maximal and average-induced slippages were 4.70 mm and 2.29 mm, respectively, with the moment magnitude M_w of the induced seismicity of 2.2380. When the permeability was 10^{-7} m/s, the maximal and average-induced slippages were 4.77 mm and 2.33 mm, respectively, with the moment magnitude M_w of the induced seismicity of 2.2427. When the permeability was 10^{-6} m/s, the maximal and average-induced slippages were 4.91 mm and 2.39 mm, respectively,

Table 11: The induced slippage and moment magnitude of fault F1 and F2 under the fracturing region area.

Experiment no.	Fault F1			Fault F2		
	Maximal slippage (mm)	Average slippage (mm)	Moment magnitude (M_w)	Maximal slippage (mm)	Average slippage (mm)	Moment magnitude (M_w)
C3A1	3.35	2.26	2.4351	1.61	1.38	2.0918
C3A2	6.02	4.05	2.6039	2.17	1.87	2.1788
C3A3	9.10	6.06	2.7203	2.69	2.10	2.2128
C3A4	12.68	8.47	2.8173	6.01	5.21	2.4756
C3A5	16.36	10.87	2.8894	7.72	6.71	2.5490

with the moment magnitude M_w of the induced seismicity of 2.2506.

The above results revealed that the slip of fault F1 and F2 obviously increased with the increase of fracturing region permeability. When the permeability increased from 10^{-10} m/s to 10^{-8} m/s, the moment magnitude M_w increased by about 0.5058. However, it had almost no increase when the permeability increased from 10^{-8} m/s to 10^{-6} m/s. The magnitude increased by only 0.0127. Figure 25 illustrates the distribution of pore pressure along the long axis of the fracturing region N1 of experiment Nos. C1K1-C1K5. The pore pressure was distributed symmetrically along the injection well (short axis of region N1) and decreased from the well to both sides. When the permeability was 10^{-10} m/s, the black curve with square symbol in Figure 25, the pore pressure decreased rapidly from the injection well to both sides. The pore pressure was 80 MPa at the midpoint (at 300 m), and rapidly decreased to 7 MPa at 220 m and 380 m and then gradually decreased to 0.7 MPa at the endpoints. With the increase of fracturing region permeability, the pore pressure on both sides of the injection well obviously increased. When the permeability increased to 10^{-8} m/s, the pore pressure at the endpoint was up to 76 MPa. When the permeability was 10^{-7} m/s and 10^{-6} m/s, the distribution of pore pressure was almost a horizontal line. It indicated that the whole fracturing region would be in high pore pressure state when its permeability was larger than 10^{-7} m/s. Therefore, when the injection pressure and time kept constant, the permeability of the fracturing region became the key factor affecting the pressure build-up in the fracturing region and the stability of fault. On one hand, enhancing the permeability of granite through hydraulic fracturing is the engineering purpose for geothermal exploitation. On the other hand, too high a permeability will threaten the stability of the site fault. In addition, the heat transfer effect will be greatly affected if the fluid flows too fast in the fracturing region. Therefore, it is needed to appropriately control the permeability of the fracturing region for a successful geothermal exploitation project.

4.3. Injection Pressure. Figures 17 and 18 and Table 9 show the results of the induced fault slippage and moment magnitude M_w of experiments Nos. C1P1-C1P5. We can see that the induced slippage of fault F1 presented similar tendency under different injection pressures. Firstly, we studied the induced fault slippage of F1 as shown in Figure 18 and Table 9. As can be seen, when injection pressure was 60 MPa to 70 MPa, 80 MPa, 90 MPa, and 100 MPa, the maximal fault slippage was 5.20 mm, 6.06 mm, 6.93 mm, 7.79 mm, and 8.66 mm, respectively. And the average slippage was 4.01 mm, 4.68 mm, 5.34 mm, 6.01 mm, and 6.67 mm, respectively. As a result, the moment magnitude M_w was 2.6007, 2.6455, 2.6837, 2.7179, and 2.7480, respectively. The results revealed that when the injection pressure was larger for 10 MPa, (1) the maximal slippage of fault F1 would increase about 0.86 mm, (2) the average slippage of fault F1 would increase about 0.66 mm, (3) and the moment magnitude M_w increased about 0.0368. Secondly, we studied the slippage of F2 as shown in Figure 18 and Table 9. When injection pressure changed from 60 MPa to 70 MPa, 80 MPa, 90 MPa, and 100 MPa, (1) the maximal fault slippage changed from 3.54 mm, 4.12 mm, 4.70 mm, 5.28 mm, and 5.85 mm, respectively; (2) the average slippage changed from 1.73 mm, 2.01 mm, 2.29 mm, 2.57 mm, and 2.85 mm, respectively; and (3) the moment magnitude M_w was 2.1566, 2.2001, 2.2378, 2.2712, and 2.3012, respectively. When injection pressure was larger for 10 MPa, the maximal and average slippage of fault F2 and the moment magnitude M_w increased about 0.58 mm, 0.28 mm, and 0.0362, respectively. The above results revealed that the induced slippage and moment magnitude of fault F1 and F2 were all evenly increased with the injection pressure. However, the increment of fault F2 was smaller than that of F1. That was because the fault rupture area of F2 was smaller than that of F1, and F2 was farther from the fracturing region N1 than F1 was.

Figure 19 illustrates the distribution of pore pressure along the major axis of region N1 under different injection pressures of experiments Nos. C1P1-C1P5. As can be seen, the pore pressure in region N1 increased with the injection pressure. The increment of pore pressure in the region was equal to the increment of injection pressure. This may explain why the induced fault slippage and moment magnitude M_w evenly increased with the injection pressure.

4.4. Area of the Fracturing Region. Figures 20 and 26 and Table 11 show the results of the induced fault slippage and moment magnitude M_w of experiments Nos. C1A1-C1A5. We can see that the induced slippage of fault F1 presented similar tendency under different areas of the fracturing region. Firstly, we studied the induced fault slippage of F1 as shown in Figure 20 and Table 11. As can be seen, when the area of the fracturing region was 0.36 A, 0.64 A, A, 1.44 A, and 1.96 A, the maximal fault slippage was 3.35 mm,

6.02 mm, 9.10 mm, 12.68 mm, and 16.36 mm, respectively. And the average slippage was 2.26 mm, 4.05 mm, 6.06 mm, 8.47 mm, and 10.87 mm, respectively. As a result, the moment magnitude M_w was 2.4351, 2.6039, 2.7203, 2.8173, and 2.8894, respectively. Secondly, we studied the slippage of F2 as shown in Figure 26 and Table 11. when the area of the fracturing region was 0.36 A, 0.64 A, A, 1.44 A, and 1.96 A, the maximal fault slippage was 1.61 mm, 2.17 mm, 2.69 mm, 6.01 mm, and 7.72 mm, respectively. And the average slippage was 1.38 mm, 1.38 mm, 1.87 mm, 2.10 mm, 5.21 mm, and 6.71 mm, respectively. As a result, the moment magnitude M_w was 2.0918, 2.1788, 2.2128, 2.4756, and 2.5490, respectively. The above results revealed that the induced slippage and moment magnitude of fault F1 and F2 were both increased with the area of the fracturing region.

5. Conclusions

The exploitation of HDR geothermal energy usually needs an enhanced geothermal system with artificial fracture networks. Hydraulic fracturing is one of the most significant technologies for making artificial fracture networks in hot dry rocks. Fault reactivation and seismicity induced by fluid injection during hydraulic fracturing often raise a great challenge because it is easy to arouse social concern. A better understanding of injection-induced fault reactivation is important for improving disaster assessment and prevention of such underground fluid injection engineering. Whether the fault is connected with fluid region or not, underground fluid injection may induce fault reactivation. However, most studies have been focused on pore pressure increase of the fault hydraulically connected to the injection. The stability of faults that are not in the pore-fluid migration region has been neglected. In this paper, the induced fault slip and seismicity characteristics during HDR geothermal exploitation were studied by a 2D numerical model by ABAQUS. The study was based on a hydraulic fracturing project in the geothermal field of Yishu fault zone of China. In this study, we focused on the faults that exist beyond the hydraulic fracturing region. The results of the study can provide some useful references for establishing HDR EGS in the Yishu fault zone. The main conclusions were as follows:

(1) Fluid injection during hydraulic fracturing can cause the fault that exist beyond the fluid-pressurized region to slip and can even induce large seismic event ($M_w \geq 3$ in our range of study)

(2) The influence of the hydraulic fracturing region on stability of fault is not simply depended on their relative spatial location of the fault and fracturing region. It was the displacement and stress disturbance induced by fluid injection in the fracturing region that ultimately caused the fault sliding instability

(3) If the fracturing region is close to the fault, as the region P1, injecting fluid into this region may induce felt seismic event. Therefore, determination of rational position of the fracturing region in an HDR EGS engineering is a key step for site stability in a hot dry rock geothermal engineering

(4) It is easier to cause felt earthquakes when hydraulic fracturing is simultaneously carried out in different layers. In the current hydraulic fracturing program, three different fracturing layers between fault F1 and F2 were set. It must be treated with caution when decided whether to carry out hydraulic fracturing in different layers at the same time

(5) When the injection pressure and time keep constant, the permeability of the fracturing region becomes the key factor affecting the pressure build-up in the fracturing region and the stability of fault. On one hand, enhancing the permeability of granite through hydraulic fracturing is the engineering purpose for geothermal exploitation. On the other hand, too high a permeability will threaten the stability of the site fault. In addition, the heat transfer effect will be greatly affected if the fluid flows too fast in the fracturing region. Therefore, it is needed to appropriately control the permeability of the fracturing region for a successful geothermal exploitation project

(6) When the fracturing region and injection time keep constant, the increment of pore pressure in the fracturing region is equal to the increment of injection pressure. As a result, the induced fault slippage and moment magnitude evenly increase with the injection pressure

(7) The induced slippage and moment magnitude of fault F1 and F2 both increase with the area of the fracturing region. In an HDR EGS engineering, the influence of the fracturing region area on the stability of the adjacent fault must be adequately assessed

Data Availability

The data used to support the findings of this study are included within the article.

Conflicts of Interest

The authors declare that they have no conflicts of interest.

Acknowledgments

The authors acknowledge the financial support from the Start-Up Fund for Doctoral Research of Suzhou University (No. 2019jb09), 2014 National Open Project of Suzhou Regional Development Collaborative Innovation Center (general) (No. 2014SZXTKF07), and University Students' Innovation and Entrepreneurship Program of Anhui Province (No. S202010379101).

References

[1] Y. Wang, Y. Liu, J. Dou, M. Li, and M. Zeng, "Geothermal energy in China: status, challenges, and policy recommendations," *Utilities Policy*, vol. 64, article 101020, 2020.

[2] Z. Feng, Y. Zhao, A. Zhou, and N. Zhang, "Development program of hot dry rock geothermal resource in the Yangbajing Basin of China," *Renewable Energy*, vol. 39, no. 1, pp. 490–495, 2012.

[3] R. M. Potter, E. S. Robinson, and M. C. Smith, *Method of extracting heat from dry geothermal reservoirs*, 1974, US Patent 3786858.

[4] Z. Zhou, Y. Jin, Y. Zeng et al., "Investigation on fracture creation in hot dry rock geothermal formations of China during hydraulic fracturing," *Renewable Energy*, vol. 153, pp. 301–313, 2020.

[5] H. Huang, T. Babadagli, X. Chen, H. Li, and Y. Zhang, "Performance comparison of novel chemical agents for mitigating water-blocking problem in tight gas sandstones," *SPE Reservoir Evaluation & Engineering*, vol. 23, no. 4, pp. 1150–1158, 2020.

[6] H. Huang, T. Babadagli, H. Li, K. Develi, and D. Zhou, "A visual experimental study on proppants transport in rough vertical fractures," *International Journal of Rock Mechanics and Mining Sciences*, vol. 134, p. 104446, 2020.

[7] K. T. Terzaghi, *Theoretical Soil Mechanics*, Wiley and Sons, New York, 1943.

[8] Y. Guglielmi, F. Cappa, J. P. Avouac, P. Henry, and D. Elsworth, "Seismicity triggered by fluid injection–induced aseismic slip," *Science*, vol. 348, no. 6240, pp. 1224–1226, 2015.

[9] S. A. Shapiro, E. Huenges, and G. Borm, "Estimating the crust permeability from fluid-injection-induced seismic emission at the KTB site," *Geophysical Journal International*, vol. 131, no. 2, pp. F15–F18, 1997.

[10] Q. Gan and D. Elsworth, "Analysis of fluid injection-induced fault reactivation and seismic slip in geothermal reservoirs," *Journal of Geophysical Research Solid Earth*, vol. 119, no. 4, pp. 3340–3353, 2014.

[11] S. A. Shapiro, E. Rothert, V. Rath, and J. Rindschwentner, "Characterization of fluid transport properties of reservoirs using induced microseismicity," *Geophysics*, vol. 67, no. 1, pp. 212–220, 2002.

[12] H. Soltanzadeh and C. D. Hawkes, "Semi-analytical models for stress change and fault reactivation induced by reservoir production and injection," *Journal of Petroleum Science & Engineering*, vol. 60, no. 2, pp. 71–85, 2008.

[13] T. Diehl, T. Kraft, E. Kissling, and S. Wiemer, "The induced earthquake sequence related to the St. Gallen deep geothermal project (Switzerland): fault reactivation and fluid interactions imaged by microseismicity," *Journal of Geophysical Research*, vol. 122, no. 9, pp. 7272–7290, 2017.

[14] B. Li, R. Bao, Y. Wang, R. Liu, and C. Zhao, "Permeability evolution of two-dimensional fracture networks during shear under constant normal stiffness boundary conditions," *Rock Mechanics and Rock Engineering*, vol. 3, pp. 1–20, 2020.

[15] M. Almakari, H. Chauris, F. Passelègue, P. Dublanchet, and A. Gesret, "Fault's hydraulic diffusivity enhancement during injection induced fault reactivation: application of pore pressure diffusion inversions to laboratory injection experiments," *Geophysical Journal International*, vol. 223, no. 3, pp. 2117–2132, 2020.

[16] Z. Fan, P. Eichhubl, and P. Newell, "Basement fault reactivation by fluid injection into sedimentary reservoirs: poroelastic effects," *Journal of Geophysical Research Solid Earth*, vol. 124, no. 7, pp. 7354–7369, 2019.

[17] J. Rutqvist, F. Cappa, A. P. Rinaldi, and M. Godano, "Dynamic modeling of injection-induced fault reactivation and ground motion and impact on surface structures and human perception," *Energy Procedia*, vol. 63, pp. 3379–3389, 2014.

[18] J. S. Yoon, A. Zang, O. Stephansson, and G. Zimmermann, "Modelling of fluid-injection-induced fault reactivation using a 2D discrete element based hydro-mechanical coupled dynamic simulator," *Energy Procedia*, vol. 97, pp. 454–461, 2016.

[19] W. W. Rubey, "Role of fluid pressure in mechanics of overthrust faulting. Parts I and II," *Geological Society of America Bulletin*, vol. 70, no. 5, p. 115, 1959.

[20] M. L. Bell and A. Nur, "Strength changes due to reservoir-induced pore pressure and stresses and application to Lake Oroville," *Journal of Geophysical Research Atmospheres*, vol. 83, no. B9, pp. 4469–4485, 1978.

[21] P. Bhattacharya and R. C. Viesca, "Fluid-induced aseismic fault slip outpaces pore-fluid migration," *Science*, vol. 364, no. 6439, pp. 464–468, 2019.

[22] T. H. W. Goebel and E. E. Brodsky, "The spatial footprint of injection wells in a global compilation of induced earthquake sequences," *Science*, vol. 361, no. 6405, pp. 899–904, 2018.

[23] S. Wei, J. P. Avouac, K. W. Hudnut et al., "The 2012 Brawley swarm triggered by injection-induced aseismic slip," *Earth and Planetary Science Letters*, vol. 422, pp. 115–125, 2015.

[24] F. Grigoli, S. Cesca, A. P. Rinaldi et al., "The November 2017Mw5.5 Pohang earthquake: a possible case of induced seismicity in South Korea," *Science*, vol. 360, no. 6392, pp. 1003–1006, 2018.

[25] K. Shan, Y. Zhang, Y. Zheng, L. Li, and H. Deng, "Risk assessment of fracturing induced earthquake in the Qiabuqia Geothermal Field, China," *Energies*, vol. 13, no. 22, article 5977, 2020.

[26] W. Gui-ling, Z. Wei, L. Ji-yun, L. Wen-jing, L. Zhi-ming, and W. Wan-li, "Evaluation of geothermal resources potential in China," *Acta Geoscientica Sinica (Chinese)*, vol. 38, no. 4, pp. 449–459, 2017.

[27] C. Lu, W. Lin, H. Gan, F. Liu, and G. Wang, "Occurrence types and genesis models of hot dry rock resources in China," *Environmental Earth Sciences*, vol. 76, no. 19, 2017.

[28] Q. Deng, A. Jiang, Z. Tong et al., "Evaluation of favourable hot dry rock areas in the east of the Yishu fault zone in China," *Australian Journal of Earth Sciences*, vol. 68, no. 2, pp. 245–261, 2021.

[29] Q. X. Meng, W. Y. Xu, H. L. Wang, X. Y. Zhuang, and T. Rabczuk, "DigiSim-an open source software package for heterogeneous material modeling based on digital image processing," *Advances in Engineering Software*, vol. 146, no. 9, p. 16, 2020.

[30] Q. Wang, H. Gao, B. Jiang, S. Li, M. He, and Q. Qin, "In-situ test and bolt-grouting design evaluation method of underground engineering based on digital drilling," *International Journal of Rock Mechanics and Mining Sciences*, vol. 138, article 104575, 2021.

[31] Q. Wang, Q. Qin, B. Jiang et al., "Mechanized construction of fabricated arches for large-diameter tunnels," *Automation in Construction*, vol. 124, no. 3, article 103583, 2021.

[32] Hibbitt, Karlsson, and Sorensen, *ABAQUS theory manual, Version 6.2*, Dassault Systemes Simulia Corp., Providence, RI, USA, 2001.

[33] M. A. Biot, "General theory of three-dimensional consolidation," *Journal of Applied Physics*, vol. 12, no. 2, pp. 155–164, 1941.

[34] J. R. Rice and M. P. Cleary, "Some basic stress diffusion solutions for fluid-saturated elastic porous media with compressible constituents," *Reviews of Geophysics and Space Physics*, vol. 14, no. 2, pp. 227–241, 1976.

[35] X. Zhou and T. J. Burbey, "Deformation characteristics of a clayey interbed during fluid injection," *Engineering Geology*, vol. 183, pp. 185–192, 2014.

[36] K. Aki, "Scaling law of seismic spectrum," *Journal of Geophysical Research Atmospheres*, vol. 72, no. 4, pp. 1217–1231, 1967.

[37] H. Kanamori and D. L. Anderson, "Theoretical basis of some empirical relations in seismology," *Bulletin of the Seismological Society of America*, vol. 65, no. 5, pp. 1073–1095, 1975.

[38] H. Kanamori, "The energy release in great earthquakes," *Journal of Geophysical Research*, vol. 82, no. 20, pp. 2981–2987, 1977.

[39] T. C. Hanks and H. Kanamori, "A moment magnitude scale," *Journal of Geophysical Research*, vol. 84, no. B5, p. 2348, 1979.

[40] Z. Tao, C. Zhu, M. He, and M. Karakus, "A physical modeling-based study on the control mechanisms of Negative Poisson's ratio anchor cable on the stratified toppling deformation of anti- inclined slopes," *International Journal of Rock Mechanics and Mining Sciences*, vol. 138, article 104632, 2021.

[41] Y. Wang, C. H. Li, H. Liu, and J. Q. Han, "Fracture failure analysis of freeze-thawed granite containing natural fracture under uniaxial multi-level cyclic loads," *Theoretical and Applied Fracture Mechanics*, vol. 110, article 102782, 2020.

[42] Q. Gan, *Analysis of Induced Seismicity and Heat Transfer in Geothermal Reservoirs by Coupled Simulation*, The Pennsylvania State University, 2015.